Characterizing network directedness using the containing pseudospectral frontier of the network Laplacian

Christopher J. Keylock
School of Architecture, Building and Civil Engineering, Loughborough University, Loughborough, United Kingdom

Maurizio Carbone
Istituto dei Sistemi Complessi, CNR, Via dei Taurini 19, 00185 Rome, Italy
and INFN "Tor Vergata", Via della Ricerca Scientifica 1, 00133 Rome, Italy

(Received 22 September 2025; accepted 5 March 2026; published 25 March 2026)

A large number of complex systems can be represented as directed networks, where the connections (edge weights) between nodes (system states) are such that the flux of the quantity of interest (e.g., energy or information) from node i to j is not equal to that from j to i. The network Laplacian underpins a suite of techniques for studying diffusion and random walks on networks, but many such methods have been developed for undirected graphs. In this paper, we propose a method for characterizing the relative degree of directedness of a network. Our approach is based on the pseudospectrum of the Laplacian and examines the difference in the nature of the "containing pseudospectral frontier" between the Laplacian itself and a variant formed by removing its non-normal structure. The distance between the containing and comparator frontiers then characterizes relative directedness as a function of the shape of the underlying pseudospectral surface. We demonstrate how this metric's behavior is consistent with that expected for a cyclic permutation adjacency matrix and is appropriate for a network where directedness is controlled systematically. We also extend an existing definition of network directedness and then apply our method in detail to a network capturing the Lagrangian dynamics of a turbulent flow. Two local maxima for our metric arise in distinct regions of the complex plane, but the eigenvalues driving these maxima are dominated by nodes from the network that are both very similar to each other and highly atypical in terms of the physics they embody. These nodes are also very different in nature from those highlighted by a stochastic differential equation model for these dynamics that successfully captures many key features of turbulence. This highlights the sensitivity of our approach and its potential utility in model validation, in addition to network characterization.

DOI: 10.1103/lbfb-69mf

I. INTRODUCTION

Networks exist as physical entities in transport [1,2], energy supply [3], and river drainage [4]), as well as serving as a means to analyze a suite of discrete processes such as social networks [5], neuron interconnectivity [6], and disease transmission [7]. Furthermore, following discretization into a suitable state vector, it is possible to analyze continuous processes using this approach [8,9]. In reality, many of these networks are directed, but network theory has traditionally been built around concepts derived for the undirected case. For example, consideration of diffusion on a network leads to analysis in terms of the network Laplacian [10], and the Cheeger constant can then be used to determine the minimum number of cuts that need to be made to partition a network into unconnected subgraphs. While there has been effort devoted to deriving Cheeger inequalities for directed graphs [11], an alternative perspective is that the Cheeger constant is innately associated with undirected graphs and that alternative approaches are needed for directed graphs [12].

A notion of directedness for the graph Laplacian is needed to underpin the development of bespoke methods for directed graph Laplacians (DGLs) and the approach we take in this paper to relative directedness is explicitly framed in the context of matrix non-normality (see [13] for another study adopting related techniques in network science). We make explicit use of the non-Hermitian nature of the directed network and its associated Laplacian to characterize directionality in terms of the pseudospectrum [14] of the Laplacian, rather than using just the eigenvalues. This means we are not restricted to using the imaginary part of the eigenvalues as a metric of directedness, but can go further and characterize how the eigenvalues interact with each other to structure the pseudospectral surface that underpins the directed nature of the Laplacian. See [14] for a number of examples of this for a range of matrices in different domains of application. In particular, we define a threshold value for the pseudospectrum, ϵ_τ, which leads to a *containing frontier* in the complex plane that encloses all of the eigenvalues of the Laplacian with respect to the real line. A comparator frontier may then be defined from the

Published by the American Physical Society under the terms of the Creative Commons Attribution 4.0 International license. Further distribution of this work must maintain attribution to the author(s) and the published article's title, journal citation, and DOI.

normal variant of the Laplacian (one with the same eigenvalues as the source Laplacian, but with the matrix non-normality removed). The distance between these two frontiers then provides a measure of relative network directedness. It is then possible to infer the extent to which the individual nodes of the network impact upon the directionality. We demonstrate the utility of our method using various examples of directed networks.

II. NETWORKS AND NETWORK LAPLACIANS

A graph or network $\mathcal{G}$ comprises a set of n nodes (vertices), edges between nodes, $\mathcal{E}$, and weights associated with each edge, $\mathcal{W}$. It is assumed throughout this article that there are no self-loops in the graph, which means that the primary diagonal of the $n \times n$ adjacency matrix $\boldsymbol{A}$ consists of zeros. An unweighted graph then has off-diagonal values of 1 where there is an edge (a direct connection) between nodes i and j. For the weighted case, the weight w_{ij} for an edge is is any non-negative value and an undirected network has $w_{ij} = w_{ji}$. The nodal out-degree $D_i^O = \sum_j w_{ij}$ and in-degree $D_j^I = \sum_i w_{ij}$ are therefore unlikely to be the same for a directed network. In this study, we work with the out-degree vector, $\overrightarrow{D}^O$, consisting of the N values, D_i^O. The associated out-degree matrix is then given by

$$\boldsymbol{D} = \boldsymbol{I} \odot (\overrightarrow{D}^O \ \overrightarrow{1}^T), \tag{1}$$

where $\boldsymbol{I}$ is the identity matrix and $\overrightarrow{1}$ is the vector of ones. The empirical probability of transitioning from node i to j (the conditional probability of reaching node j given one is at node i) is then given by $P_{ij} = w_{ij}/D_i^O$, which in matrix form for all nodes is given by

$$\boldsymbol{P} = \boldsymbol{D}^{-1}\boldsymbol{A}. \tag{2}$$

In this study, we work with strongly connected graphs where a path may be constructed from any node to any other node. This is important as it means the stationary probability vector $\overrightarrow{S}$ is not singular, and hence $\overrightarrow{S} = \overrightarrow{S}\boldsymbol{P}$, where $\overrightarrow{S}$ is given by the left eigenvector of $\boldsymbol{P}$ that corresponds to the eigenvalue of $\boldsymbol{P}$ with a value of 1. The vector $\overrightarrow{S}$ may be placed in matrix form in an analogous manner to (1).

Network Laplacians

Diffusion on a network is determined using a network Laplacian and a variety of Laplacians have been proposed for a number of different purposes. The most commonly applied one for undirected networks is the unnormalized network Laplacian,

$$\boldsymbol{L}_u = \boldsymbol{D} - \boldsymbol{A}, \tag{3}$$

which has been used to identify nodes with a high network centrality [15] and to underpin spectral graph partitioning methods [16]. Another relevant Laplacian is the ordinary Laplacian,

$$\boldsymbol{L}_{\text{ord}} = \boldsymbol{S}(\boldsymbol{I} - \boldsymbol{P}), \tag{4}$$

although its primary use for directed graphs has been in its symmetrized form,

$$\boldsymbol{L}_s = (\boldsymbol{L}_{\text{ord}} + \boldsymbol{L}_{\text{ord}}^*)/2, \tag{5}$$

where the asterisk is the conjugate transpose. A normalized Laplacian for directed graphs (henceforth, the digraph Laplacian or DGL) was introduced by [12] and given by

$$\boldsymbol{\mathcal{L}} = \boldsymbol{I} - \boldsymbol{S}^{\frac{1}{2}}\boldsymbol{P}\boldsymbol{S}^{-\frac{1}{2}}, \tag{6}$$

where the vector $\overrightarrow{S}^{\frac{1}{2}}$ used to form $\boldsymbol{S}^{\frac{1}{2}}$ consists of elements $\sqrt{S_i}$. It was proven by [12] that this Laplacian can be used to solve the Laplace equation for diffusion on a network and, thus, provide the hitting times and commute times on the network, i.e., the expected time to move from node i to j or the expected time to move from node i back to i via node j [17]. Given that it provides a formally correct means to analyze diffusion on directed networks, we adopt the DGL given by (6) in this study.

III. PSEUDOSPECTRA, THE CONTAINING FRONTIER AND CHARACTERIZING DIRECTEDNESS

The application of non-normality and associated pseudospectral concepts to complex networks has been relatively limited, although Ref. [13] introduced a number of relevant concepts and applied them to the adjacency matrix. A key result of their study was that the hierarchical nature of preferential attachment methods for building a network [18] resulted in greater non-normality to the network structure than the use of Erdös-Rényi [19] or Watts-Strogatz [20] methods for network construction. Given that many networks have been shown to exhibit a hierarchical nature (e.g., [21,22]), using the pseudospectrum to characterize the non-normality of the network would appear to be a profitable avenue to explore. In contrast to [13], we focus on the directed graph Laplacian (DGL) rather than the adjacency matrix. The DGL provides a normalized space for studying network structure as all eigenvalues sit on or within a unit circle with origin $1 + 0i$. Because all the entries in $\boldsymbol{A}$ are real valued, eigenvalues are either real or come in conjugate pairs, meaning that analysis using the half circle is sufficient.

A. Definition of pseudospectra

A number, $z\lambda \in \mathcal{C}$ is an eigenvalue of a matrix $\boldsymbol{\mathcal{L}}$, if $z\boldsymbol{I} - \boldsymbol{\mathcal{L}}$ is singular. This leads to the definition of the resolvent of $\boldsymbol{\mathcal{L}}$ at z as $(z\boldsymbol{I} - \boldsymbol{\mathcal{L}})^{-1}$, and the pseudospectrum $\Lambda_\epsilon(\boldsymbol{\mathcal{L}})$[14] then follows,

$$\Lambda_\epsilon(\boldsymbol{\mathcal{L}}) = \|(z\boldsymbol{I} - \boldsymbol{\mathcal{L}})^{-1}\| \geqslant \epsilon^{-1}, \tag{7}$$

for $\epsilon \geqslant 0$. With $\|(z\boldsymbol{I} - \boldsymbol{\mathcal{L}})^{-1}\| = \infty$ if $z \in \Lambda(\boldsymbol{\mathcal{L}})$, i.e., where z corresponds to the location of an eigenvalue of $\mathcal{L}$, for $\epsilon > 0$, the pseudospectrum can be considered as the part of the complex plane within a bounding contour, the area of which increases with ϵ. An equivalent expression to (7) in a Hilbert space setting that hints at the computational means for determining the pseudospectrum is

$$\Lambda_\epsilon(\boldsymbol{\mathcal{L}}) = \sigma_{\min}(z\boldsymbol{I} - \boldsymbol{\mathcal{L}}) \leqslant \epsilon, \tag{8}$$

where $\sigma_{\min}$ is the smallest singular value of $z\boldsymbol{I} - \boldsymbol{\mathcal{L}}$. For a normal matrix such as $\boldsymbol{\mathcal{L}}_s$ where $\boldsymbol{\mathcal{L}}\boldsymbol{\mathcal{L}}^* = \boldsymbol{\mathcal{L}}^*\boldsymbol{\mathcal{L}}$, $\Lambda_\epsilon(\boldsymbol{\mathcal{L}})$ is simply the points in the complex plane that are within the distance ϵ of the spectrum. For non-normal matrices, this distance can be much larger [23], resulting in imprecise analyses of non-normal matrices using eigenvalue-based methods. An important example of this is given in Refs. [24,25], in which the plane Poiseuille flow between parallel plates was studied, using the Orr-Sommerfeld (OS) operator, and the discrepancy between experimental values for the transition to turbulence at a critical Reynolds number of $\sim$1000 and analytical calculations that stated this should arise at a value of 5772 was explained [26]: For a Reynolds number of $1000 \lesssim \mathrm{Re} < 5000$, physically relevant contours of the pseudospectrum already protruded into the upper half plane, although the eigenvalues retained a negative imaginary part.

B. Defining a pseudospectral threshold and frontier

The field of values or numerical range, $W(\boldsymbol{\mathcal{L}})$, may be used to define a variety of scalar quantities for characterizing the spectrum of a matrix, and these in turn have analogies for the pseudospectrum, as described in Appendix A. The pseudospectral variants may be converted into vector quantities by treating them as a function of ϵ, but this would require a significant degree of computation. Hence, in this paper, we use a single, threshold choice for ϵ and define our quantities relative to this. We refer to this as τ_ϵ and, subsequently, we indicate this with a τ subscript in our notation with the understanding that we are working with ϵ with a value of τ_ϵ. This value will itself be an important property of the directedness of the DGL, but also permits us to characterize the pseudospectrum in relation to the contour associated with τ_ϵ.

Noting that the symmetrized Laplacian or the Laplacian for an undirected graph has real eigenvalues, we define the *containing pseudospectral frontier* as the z_τ contour, where

$$\tau_\epsilon = (\sup \epsilon) + \delta \;\text{ for }\; \min \mathrm{Re}(\Lambda) < z < \max \mathrm{Re}(\Lambda), \quad (9)$$

where δ is a small value to deal with machine precision during the calculation. As this definition ensures that no larger value than τ_ϵ occurs between the eigenvalues on the real line, z_τ may be interpreted as the smallest contour in the complex plane that bounds all the eigenvalues for the Laplacian on the real line. Hence, this choice is readily interpretable because any smaller value results in a separation of the eigenvalues into subnetworks based on a partition on the real line. Practical calculation is undertaken by choosing a number of discrete points for $\min \mathrm{Re}(\Lambda) < z < \max \mathrm{Re}(\Lambda)$ and then obtaining the corresponding value for ϵ using the inverse Lanczos algorithm of [27]. We then interpolate along this line to find τ_ϵ. Working on the real line is computationally efficient compared to two-dimensional approaches for the full pseudospectrum [28], which is of practical importance when working with large matrices.

C. The definition of a comparator frontier

Pseudospectra are closely related to the matrix nearness problem [29]. An example is that of finding the closest normal matrix, a process used for developing stable control strategies [30,31]. The normality of a matrix may be expressed in a number of ways, including $\boldsymbol{\mathcal{L}}\boldsymbol{\mathcal{L}}^* = \boldsymbol{\mathcal{L}}^*\boldsymbol{\mathcal{L}}$, as noted above. Because a normal matrix has orthonormal eigenvectors, this is equivalent to

$$\boldsymbol{U}\boldsymbol{\Lambda}\boldsymbol{U}^* = \boldsymbol{E}\boldsymbol{\Lambda}\boldsymbol{E}^{-1}, \quad (10)$$

where $\boldsymbol{E}$ are the right eigenvectors of $\boldsymbol{\mathcal{L}}$, which are associated with a diagonal matrix of eigenvalues, $\boldsymbol{\Lambda}$. The unitary Schur vectors $\boldsymbol{U}$ are associated to the inner Schur matrix from a complex Schur decomposition [32] according to

$$\begin{aligned} \boldsymbol{U}\boldsymbol{T}\boldsymbol{U}^* &= \boldsymbol{\mathcal{L}}, \\ \boldsymbol{T} &= \boldsymbol{\Lambda} + \boldsymbol{N}, \end{aligned} \quad (11)$$

where the upper triangular Schur matrix $\boldsymbol{T}$ is decomposed into a diagonal matrix of eigenvalues and a strictly upper triangular non-normality matrix $\boldsymbol{N}$. That is, (10) holds true when $\|\boldsymbol{N}\| = 0$; there is no non-normality [23].

Based on these ideas, a comparator frontier may be formulated from the normal variant of $\boldsymbol{\mathcal{L}}$ by undertaking a complex Schur decomposition according to (11), discarding $\boldsymbol{N}$ and reconstituting the matrix,

$$\boldsymbol{\mathcal{L}}_n = \boldsymbol{U}\boldsymbol{\Lambda}\boldsymbol{U}^*. \quad (12)$$

Clearly, $\boldsymbol{\mathcal{L}}_n$ has the same spectrum as $\boldsymbol{\mathcal{L}}$, but as it is normal, $z_\tau(\boldsymbol{\mathcal{L}}_n)$ is simply the set of points that lies a distance τ_ϵ from the spectrum. Hence, this frontier and that defined in (9) are both based on τ_ϵ, but the comparator frontier excludes the effect of directedness due to the non-normality of the DGL. A distance between the two then provides a means to characterize relative directedness.

D. The use of a displaced origin

We obtain z_τ using a bisection search algorithm [33], adopted to a pseudospectral context by [34]. For compactness, this is explained in more detail in Appendix B. However, an important practical point is that this is a radial calculation based on the angles in the half circle, $\theta_j \in \{0, \pi\}$. However, we know for the DGL that there will be an eigenvalue at the origin and, therefore, the influence of this eigenvalue will dominate the calculation, resulting in less precise estimation for the rest of the frontier. The solution we adopt is to redefine the origin at $1 + 0i$, i.e., the center of the unit circle that contains the spectrum, and to define angles θ_0 from this origin [as can be seen in in Figs. 1(b) and 1(c)]. This is equivalent to analyzing a displaced Laplacian, $\boldsymbol{\mathcal{L}} - \boldsymbol{I}$.

IV. DIRECTEDNESS METRICS

To illustrate the concepts introduced so far, we commence by considering the cyclic permutation matrix mentioned above, i.e., a matrix with adjacency matrix given by

$$\boldsymbol{A}_{\mathrm{cpm}} = \begin{bmatrix} 0 & 1 & \cdots & \cdots & 0 \\ 0 & 0 & 1 & \cdots & 0 \\ \vdots & \vdots & \vdots & \ddots & \vdots \\ 0 & 0 & 0 & \cdots & 1 \\ 1 & 0 & 0 & \cdots & 0 \end{bmatrix}. \quad (13)$$

We also study a directed cat cerebral cortex network consisting of 65 nodes and 1139 edges [35–37]. Figure 1(a) shows

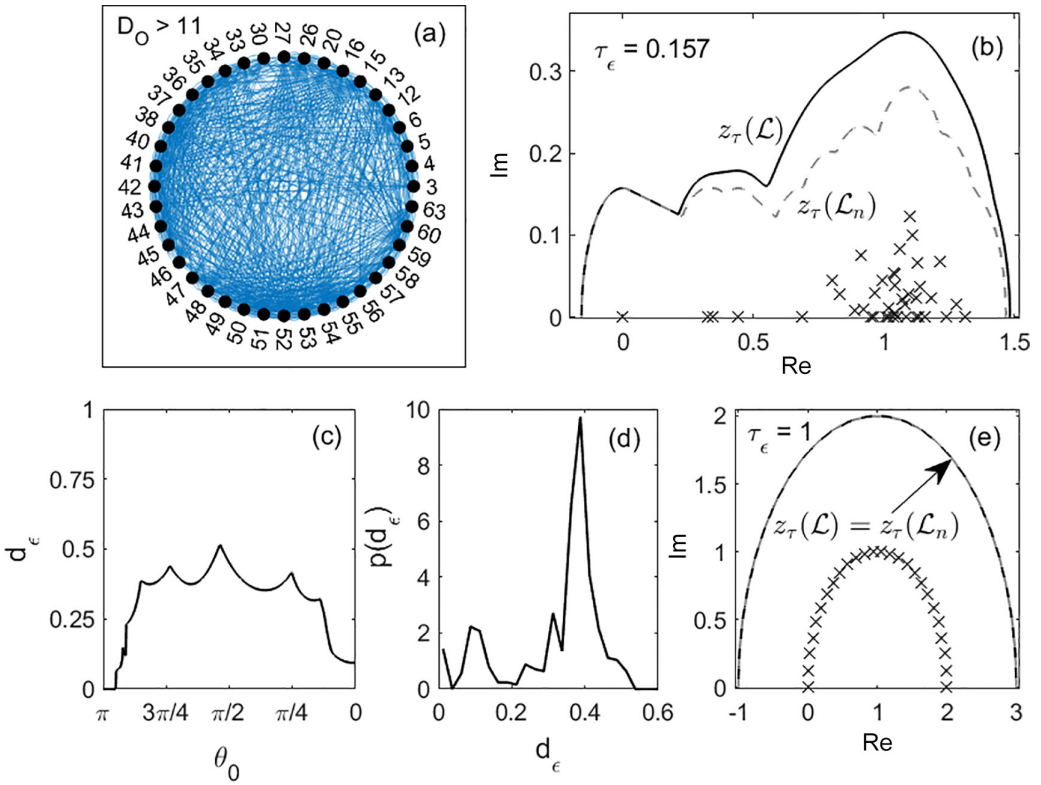


FIG. 1. The containing pseudospectral and comparator frontiers for the DGL of (b) an unweighted cat cerebral cortex network [35] and (e) a cyclic permutation matrix. The cortex network is shown in (a) for nodes with out-degree, D_i^O, greater than 11. The DGL eigenvalues (crosses) and containing frontiers at $\tau_\epsilon = 0.157$ are shown in (b). The black line is the containing pseudospectral frontier, $z_\tau(\mathcal{L})$, and the gray dashed line is the comparator frontier, $z_\tau(\mathcal{L}_n)$. (c) shows d_ϵ as a function of the angle from the displaced origin, θ_0, while (d) is a histogram of d_ϵ. In (e), the two frontiers are equal (hence, $d_\epsilon = 0$), and $\tau_\epsilon = 1$ for the cyclic permutation matrix.

the interconnectivity between the cat cortex nodes with greatest out-degree. Figure 1(b) shows the upper half plane with eigenvalues for $\mathcal{L}$ as crosses. The containing frontier $z_\tau(\mathcal{L})$ is given by a solid black line and the comparator frontier $z_\tau(\mathcal{L}_n)$ is given by a gray dashed line. That the threshold condition equates to $\tau_\epsilon = 0.157$ is implied by the distance of both frontiers from the isolated eigenvalue at the origin. Figure 1(e) is the equivalent to Fig. 1(b) for $\boldsymbol{A}_{\text{cpm}}$ and here the eigenvalues are on the edge of the unit circle, the two frontiers are equal (the DGL for this case has no non-normality), and $\tau_\epsilon = 1$ (the two frontiers are a circle with a radius of 2). Hence, this case is a useful "toy model" because it has directedness (nonzero imaginary part to the eigenvalues) but no relative directedness (no non-normality to the DGL).

Directedness metrics may be formed in the space of the pseudospectrum given in Figs. 1(b) and 1(e) using scalar quantities such as the pseudospectral ordinate explained in Appendix A. The pseudospectral ordinates (A6) for the two frontiers in Fig. 1(b) are $\beta_\tau(\mathcal{L}) = 0.347$ and $\beta_\tau(\mathcal{L}_n) = 0.280$, with the latter value following from the sum of $\tau_\epsilon = 0.157$ and $\max[\text{Im}(\Lambda)] = 0.123$. In Fig. 1(e), we have that $\beta_\tau(\mathcal{L}) = \beta_\tau(\mathcal{L}_n) = 2$; the radius of a circle as far again from the eigenvalues as the eigenvalues are from the displaced origin. Thus, relevant absolute and relative directedness metrics follow as

$$\text{Directedness (1)} : \beta_\tau(\mathcal{L}), \tag{14}$$

leading to

$$\text{Relative Directedness (1)} : \beta_{\text{ex}} = \frac{\beta_\tau(\mathcal{L}) - \beta_\tau(\mathcal{L}_n)}{\beta_\tau(\mathcal{L}_n)}, \tag{15}$$

with $\beta_{\text{ex}} = 0.24$ for the cat cerebral cortex example and $\beta_{\text{ex}} = 0$ for $\boldsymbol{A}_{\text{cpm}}$.

Scalar quantities such as β_{ex} characterize the DGL by an extreme position. An alternative is to capture information on the shapes of the frontiers as a whole. Noting that the distribution for ϵ is strongly nonlinear over the surface underpinning the contours in Fig. 1(b), it is a dramatic simplification to, for example, adopt the difference in the imaginary part of the two frontiers as a metric. Hence, we evaluate ϵ for the source DGL, $\mathcal{L}$, on the comparator threshold contour, $z_\tau(\mathcal{L}_n)$. We can then produce a relative measure for directedness, d_ϵ, based on the values for ϵ on both frontiers,

$$d_\epsilon(\theta_0) = \frac{\tau_\epsilon - \epsilon(\mathcal{L} \to \mathcal{L}_n)}{\tau_\epsilon},$$
$$\epsilon(\mathcal{L} \to \mathcal{L}_n) = \epsilon(\mathcal{L}) \quad \forall\, z \in z_\tau(\mathcal{L}_n), \tag{16}$$

where $z_\tau(\mathcal{L}_n)$ is determined as a function of θ_0. The $d_\epsilon(\theta_0)$ values for the cat cerebral cortex are shown as a function of θ_0 in Fig. 1(c), while $d_\epsilon = 0$ for $\boldsymbol{A}_{\text{cpm}}$ as is clear visually from Fig. 1(e) due to the occluded nature of the two frontiers. The histogram of d_ϵ from Fig. 1(c) is given in Fig. 1(d). It is clear from these two panels that d_ϵ is non-Gaussian, implying the use of a mean value to summarize the behavior will be biased

towards the zero values that will arise for large θ_0. Thus, the median or mode are more suitable statistics and, for the cat network, we have a median of $\langle d_\epsilon \rangle_{50} = 0.37$, a mode of 0.38, and a maximum of $\max(d_\epsilon) = 0.515$. Hence, for reasons of ease of computation, we propose that a summary scalar metric for relative directedness is based on the median,

$$\text{Relative Directedness (2)} : \langle d_\epsilon \rangle_{50}. \tag{17}$$

Analysis of an existing formulation for directedness

Noting that a set of digraphs can have the same symmetrized Laplacian (5), it was proposed by [12] to consider the antisymmetric Laplacian

$$\mathcal{L}_a = \tfrac{1}{2}(\mathcal{L} - \mathcal{L}^*), \tag{18}$$

and use its largest singular value, $\sigma_{\max}(\mathcal{L}_a)$, as a measure of directedness,

$$\text{Directedness(2)} : \sigma_{\max}(\mathcal{L}_a). \tag{19}$$

For the example in Fig. 1(b), $\sigma_{\max}(\mathcal{L}_a) = 0.252$, while, intuitively, $\sigma_{\max}(\mathcal{L}_a) = 1$ in Fig. 1(e).

The Frobenius norm of $\mathcal{L}_a$ can be expressed in terms of the norms of the imaginary part of the normal variant of $\mathcal{L}$ and the non-normality of $\mathcal{L}$ as

$$\|\mathcal{L}_a\|_F^2 = \|\text{Im}(\mathbf{\Lambda})\|_F^2 + \tfrac{1}{2}\|\boldsymbol{N}\|_F^2 \tag{20}$$

or

$$\begin{aligned}\sum \sigma(\mathcal{L}_a)^2 &= \sum \text{Im}(\mathbf{\Lambda})^2 + \frac{1}{2}\sum \sigma(\boldsymbol{N})^2 \\ &= \sum \sigma(\mathbf{\Lambda}_a)^2 + \frac{1}{2}\sum \sigma(\boldsymbol{N})^2,\end{aligned} \tag{21}$$

where $\mathbf{\Lambda}_a = \frac{1}{2}(\mathbf{\Lambda} - \mathbf{\Lambda}^*)$. In the case of the cyclic permutation matrix in Fig. 1(e), we have $\sum \sigma(\mathcal{L}_a)^2 = \sum \text{Im}(\mathbf{\Lambda})^2 = n/2$, there is no DGL non-normality, and $\sigma_{\max}(\mathcal{L}_a) \to 1$ as $n \to \infty$, explaining our earlier result for this matrix. However, in real networks, differing distributions for the singular values for $\mathcal{L}_a$ and $\boldsymbol{N}$, or the imaginary part of the eigenvalues, $\mathbf{\Lambda}$, means that it does not always follow that $\sigma_{\max}(\mathcal{L}_a)^2 > \frac{1}{2}\sigma_{\max}(N)^2$. Hence, we modify (19) to

$$\text{Directedness(2b)} : \max\left\{\sigma_{\max}(\mathcal{L}_a),\ \sqrt{\frac{1}{2}}\,\sigma_{\max}(N)\right\}. \tag{22}$$

An example where this new definition is relevant comes from the cat network in Figs. 1(a)–1(d), where $\sum \sigma(\mathcal{L}_a)^2 = 0.6821$, $\sum \text{Im}(\mathbf{\Lambda})^2 = 0.1280$, and $\frac{1}{2}\sum \sigma(\boldsymbol{N})^2 = 0.5541$. While $\sigma_{\max}(\mathcal{L}_a) = 0.252$, the other contribution is greater: $(0.5)^{0.5}\sigma_{\max}(N) = 0.2770$. We summarize various metrics for directedness applied to the cat network in Table I.

TABLE I. Directedness metrics applied to the cat cerebral cortex model due to [35].

Metric	Equation	Value
Directedness (1)	(14)	0.347
Directedness (2)	(19)	0.252
Directedness (2b)	(22)	0.277
Relative directedness (1)	(15)	0.240
Relative directedness (2)	(17)	0.369

V. TESTING AND APPLICATIONS

A. Behavior of the metrics for a perturbed network of social interaction

Having illustrated our method for a case with directedness but no relative directedness (the cyclic permutation matrix), and an example real network, in this section we first explore how different directedness metrics respond when the DGL for a network is altered in a systematic way. We then study a network in detail to highlight the physics revealed by applying $d_\epsilon(\theta_0)$ (16). An example adopted by [12] was a network of social interactions [38], the transition probability matrix for which was perturbed using a linear mixing methodology based on a control parameter, $0 \leqslant \gamma \leqslant 1$:

$$\boldsymbol{P}'(\gamma) = \gamma \boldsymbol{P} + (1-\gamma)\boldsymbol{S}^{-1}\boldsymbol{P}^*\boldsymbol{S}. \tag{23}$$

Given $\boldsymbol{P}'(\gamma)$, one can then obtain the corresponding Laplacian $\mathcal{L}'(\gamma)$ using (6). Note that the perturbation γ does not alter the eigenvalue structure, which dominates the nature of ϵ on the real line. Hence, τ_ϵ is approximately constant for all perturbations and these values are quoted in each panel of Fig. 2, which shows the eigenvalues, containing and comparative frontiers for five choices of γ.

For $\gamma = 0.5$ in Fig. 2(a), we have a DGL with no non-normality, which means that all metrics but $\beta_\tau(\mathcal{L})$ are zero in Fig. 3. This figure shows absolute (black or gray) and relative directedness (red) as a function of γ. Because the removal of non-normality from the Laplacian does not change the adjacency matrix to an undirected state, the pseudospectral ordinate $\beta_\tau(\mathcal{L})$ is nonzero at the origin. As γ increases, there is a direct proportionality between Directedness 1 [$\beta_\tau(\mathcal{L})$, black line] and Directedness 2 [$\sigma_{\max}(\mathcal{L}_a)$, gray line], with the latter only modified slightly if Directedness 2b is adopted (gray dot-dashed line). The metric that fails to increase monotonically with γ is Relative Directedness 1 (β_{ex}, red dotted line). The reason this is less successful than $\langle d_\epsilon \rangle_{50}$ (red dashed line) can be seen in Fig. 2(b): At $\gamma = 0.61$, there is an initial development of what becomes the "primary lobe" in the frontier for $\mathcal{L}$, without a significant change in $\mathcal{L}_n$ from $\gamma = 0.5$. This drives a large relative difference between $\beta_\tau(\mathcal{L})$ and $\beta_\tau(\mathcal{L}_n)$. However, by $\gamma = 0.75$ in Fig. 2(c), $\mathcal{L}_n$ has adjusted, decreasing the relative difference and weakening any association between $\beta_\tau(\mathcal{L})$ and γ. In contrast, because $\langle d_\epsilon \rangle_{50}$ incorporates information on the whole shape of the frontiers rather than just the pseudospectral ordinates, it is more robust to such changes. There is, however, a slight inflection in the results for $\langle d_\epsilon \rangle_{50}$ at $\gamma \sim 0.77$. This is due to the relatively greater development in the comparator frontier for $0.75 < \gamma < 0.8$, as seen in Figs. 2(c)–2(d).

B. A network describing the small-scale dynamics of homogeneous, isotropic turbulence

Keylock and Carbone [9] introduced a network for analyzing the Lagrangan dynamics of small-scale incompressible turbulence. Each node was defined by the unique coordinates for a state-space vector representing the signs and magnitudes of the constituents of the second and third principal invariants of the turbulent velocity gradient tensor (the first invariant is

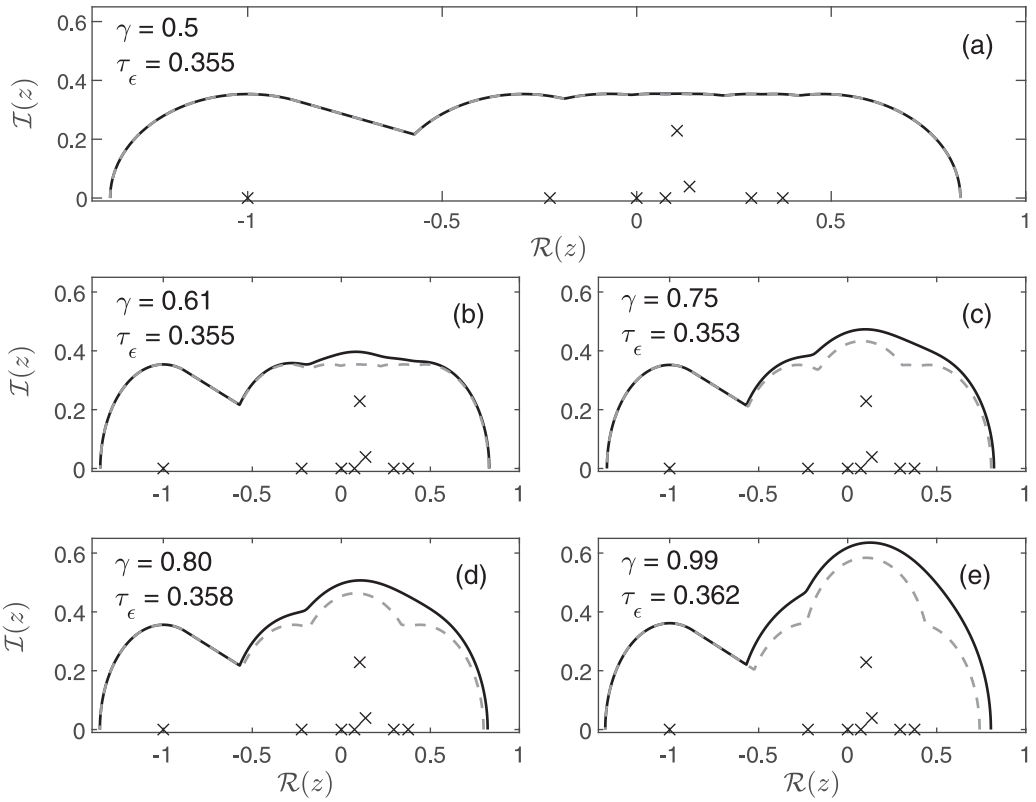


FIG. 2. The containing pseudospectral frontiers for perturbed variants of the Knoke social network [38] as a function of the control parameter, γ. Eigenvalues are given as crosses, the containing frontier for $\boldsymbol{\mathcal{L}}$ is a black line, and for $\boldsymbol{\mathcal{L}}_n$ is a dashed gray line.

zero for incompressible turbulence due to the zero divergence constraint). The various components of the state-space vector are given in the left-hand column of Table II. The second principal invariant Q concerns the difference between the

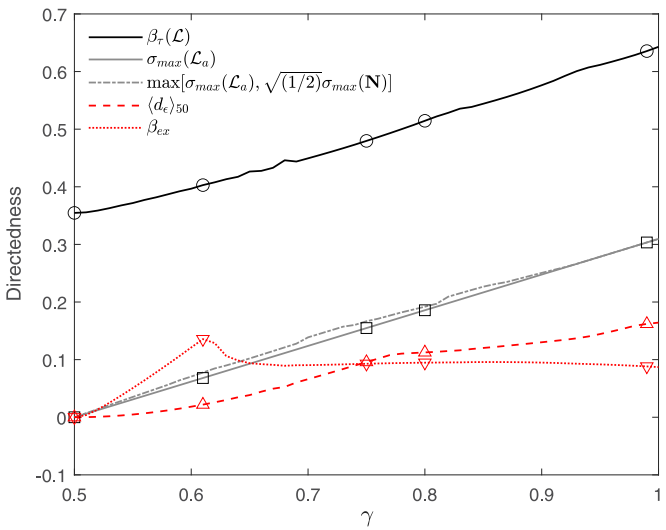


FIG. 3. Values for the directedness metrics as a function of the perturbation parameter, γ, for the Knoke social network [38]. The symbols correspond to values for γ illustrated in Fig. 2, but are not added to the line for directedness type 2b (dot-dashed gray line) for clarity given the proximity to directedness 2 (solid gray line with squares).

enstrophy $\|\boldsymbol{\Omega}\|^2$ and total strain $\|\boldsymbol{S}\|^2$, while the third, R, is the difference in strain production, $-\det(\boldsymbol{S})$, and enstrophy production, $\mathrm{tr}(\boldsymbol{\Omega}^2\boldsymbol{S})$, where $\|\cdot\|$ is the Frobenius norm, $\mathrm{tr}(\cdot)$ is the trace operator, and $\det(\cdot)$ is the determinant. These constituents were, in turn, expanded using the Schur decomposition framework [39] and in the notation below, a "B" subscript is the normal (eigenvalue-related) part of a given quantity and a "C" subscript is the non-normal part. Considering all possible combinations of the signs and magnitudes of the resulting terms gave 848 states. However, Ref. [9] found that four of these states required an alignment structure that was highly unlikely to arise in practice such that when ranked by out-degree, the 845th node was five times less likely to be reached than the 844th node. Consequently, the network was reduced to 844 nodes. The weightings for each of the edges were populated using a direct numerical simulation of homogeneous, isotropic turbulence and we compare this to the network formed by weighting the edges according to the output from the enhanced Gaussian closure (EGC) model of [40], which is a stochastic differential equation that models the Lagrangian dynamics in Q-R space.

The DGL eigenvalues and the two frontiers are shown in Figs. 4(a)–4(c), with the direct numerical simulation (DNS) results in Fig. 4(a) and those for the EGC model in Fig. 4(b), with an enlargement in Fig. 4(c). Plots of $d_\epsilon(\theta_0)$ for the respective values of τ_ϵ, stated in Figs. 4(a) and 4(b), are given in Figs. 4(d) and 4(e). Two local maxima are singled out in each of these panels as indicated by the black symbols, which are then also included in Figs. 4(a) and 4(b).

TABLE II. Properties of the state-space vectors for the network nodes most strongly weighted on the eigenvectors for the eigenvalues that drive the maximal positions for $d_\epsilon(\theta_0)$ [the eigenvalues highlighted by open symbols in Figs. 4(a)–4(c)]. The sets of integers in square brackets on rows 2 and 5 indicate the descending rank order of the magnitudes of the terms given in the first column.

	Node designation					
	DNS nodes		EGC nodes			
Property	◊	□	+	×	☆	∗
sgn[Q, R, Δ][a]	[+,−,+]	[+,−,+]	[+,+,+]	[+,+,+]	[−,−,+]	[−,−,+]
[$\|\boldsymbol{\Omega}_B\|^2$, $\|\boldsymbol{S}_B\|^2$, $\|\boldsymbol{\Omega}_C\|^2$]	[1,3,2]	[1,3,2]	[1,3,2]	[1,3,2]	[3,2,1]	[3,2,1]
sgn[$-\det(\boldsymbol{S})$, $\mathrm{tr}(\boldsymbol{\Omega}^2\boldsymbol{S})$]	[−,−][b]	[−,+][b]	[+,−]	[−,−]	[−,−]	[−,+]
sgn[$-\det(\boldsymbol{S}_C)$, $\mathrm{tr}(\boldsymbol{\Omega}_C^2\boldsymbol{S}_B)$]	[−,+]	[−,+]	[+,+]	[−,−]	[−,+]	[−,+]
[$\|\boldsymbol{SSS}_B\|$, $\|\boldsymbol{\Omega}_B^2\boldsymbol{S}_B\|$, $\|\boldsymbol{SSS}_C\|$, $\|\boldsymbol{\Omega}_C^2\boldsymbol{S}_B\|$] [c]	[4,2,1,3]	[4,2,1,3]	[4,1,2,3]	[4,1,2,3]	[1,3,2,4]	[1,3,4,2]

[a] Δ is the discriminant for the velocity gradient tensor and is $\Delta = Q^3 + (27/4)R^2$ for incompressible turbulence.
[b] The only point of difference between ◊ and □.
[c] For compactness, the determinant and trace operators have been removed from the notation here. Hence, $|\boldsymbol{SSS}_C| \equiv |\det(\boldsymbol{S}_C)|$ and $|\boldsymbol{\Omega}_B^2\boldsymbol{S}_B| \equiv |\mathrm{tr}(\boldsymbol{\Omega}_B^2\boldsymbol{S}_B)|$.

There is a marked contrast in the nature of the DGLs obtained from the DNS and the EGC, with the former yielding eigenvalues with a relatively large imaginary part, but a frontier that does not extend too much beyond them, resulting in $\tau_\epsilon = 0.0286$. However, there is a large separation between $z_\tau(\mathcal{L})$ and $z_\tau(\mathcal{L}_n)$, as seen by an average value of $\langle d_\epsilon \rangle_{50} = 0.77$. In contrast, the eigenvalues for the EGC have a small imaginary part, but the two frontiers extend much further along the imaginary axis, although they are very similar in value. Consequently, $d_\epsilon < 0.1$ for all θ_0. Given the qualitative similarity between the joint distribution functions for Q and R obtained from models of this type and the DNS, although with known limitations in the representation of the physics [40,41], our pseudospectral approach clearly provides a sensitive means to discriminate between the stochastic model and Navier-Stokes simulation.

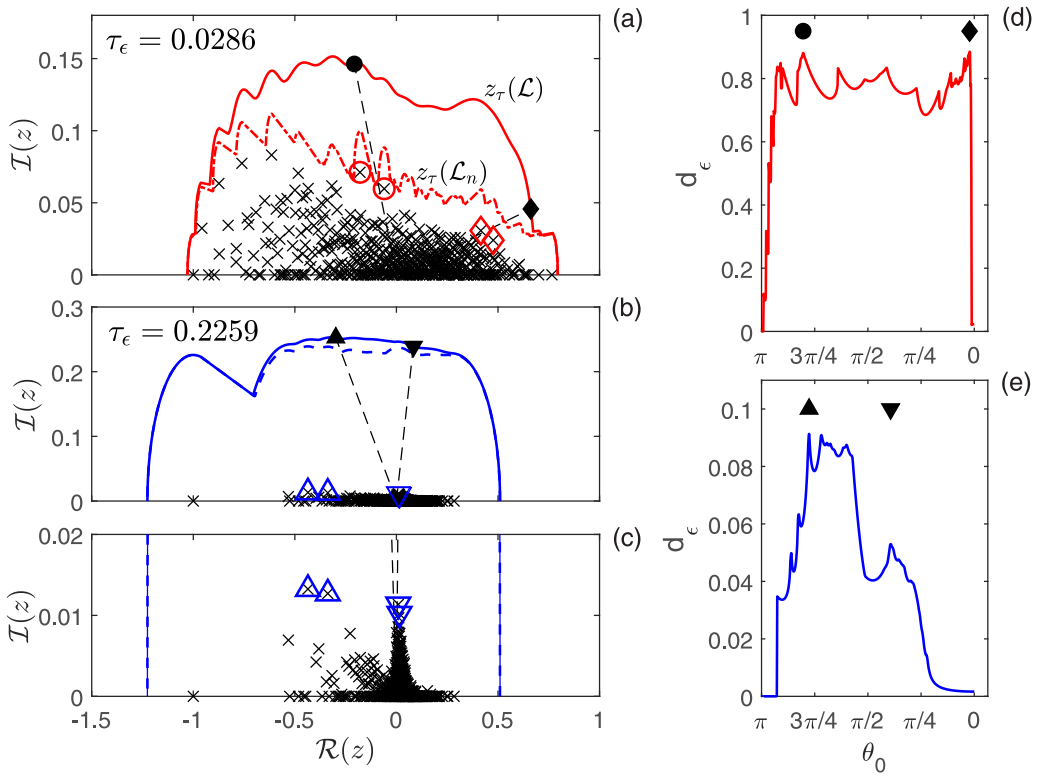


FIG. 4. The containing pseudospectral frontiers for the turbulence network due to [9] is shown in red in (a), with the network formed from the enhanced Gaussian closure shown in blue in (b) and enlarged in (c). The distance metric d_ϵ is shown as a function of θ_0 in (d) and (e) for the cases in (a) and (b), respectively. The black crosses indicate the eigenvalues, the containing frontier $z_\tau(\boldsymbol{\mathcal{L}})$ is a solid line, that for $z_\tau(\boldsymbol{\mathcal{L}}_n)$ is a dashed line, and the value for τ_ϵ is stated in the top-left corner of (a) and (b). There are two local maxima for d_ϵ in both (d) and (e) highlighted by black symbols. These are projected back onto the frontiers in (a) to (c) as highlighted by the dashed lines from the origin. The eigenvalues furthest from the origin and closest to these local maxima are highlighted by red and blue open symbols in (a) and (b), respectively.

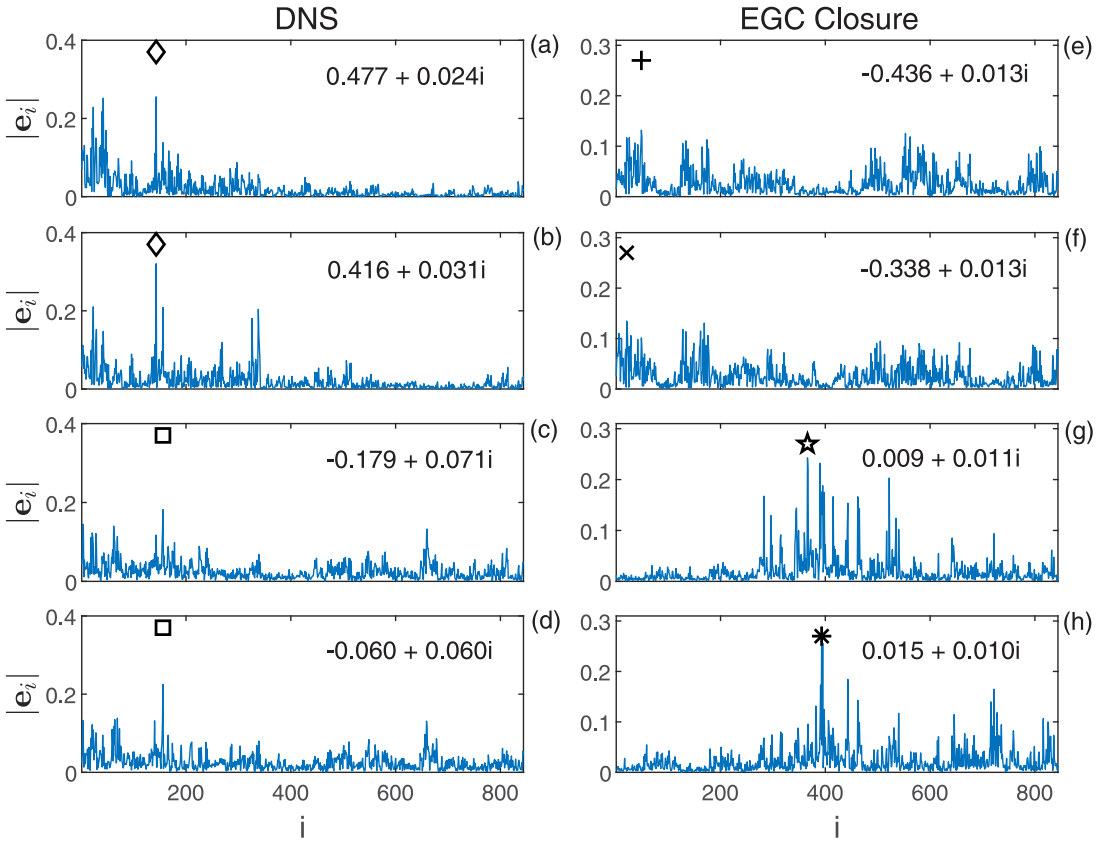


FIG. 5. The absolute values of the eigenvectors associated with the eigenvalues highlighted by circles and triangles in Fig. 4(a) are shown in the left column. The values for these eigenvalues are stated in each panel. Those associated with the highlighted eigenvalues in Fig. 4(b) are given in the right column. The symbols indicate the location of the largest magnitude term in each eigenvector (the most important node on that eigenvector). These nodes are identified by the same symbols in Table II. A repeated use of the same symbols arises because the same node in the original network is identified in these cases.

Figures 4(a) and 4(d) show that the two local maxima for d_ϵ for the DNS (black circle and diamond) appear to be driven by the behavior of two pairs of eigenvalues, highlighted by red circles and diamonds, respectively in Fig. 4(a). The absolute part of the eigenvectors, $|\boldsymbol{e}_i|$, for each of these eigenvalues was used as a means to weight the influence of each network vertex on the selected eigenvalues. These values for the DNS are shown in the left-hand column of Fig. 5, where the coordinates for the respective eigenvalues from Fig. 4 are stated in each panel. For the two pairs of eigenvalues highlighted in Fig. 4(a), the same node was the highest weighted for both members of the pair, and these are shown by a diamond and square, respectively. Remarkably, given the very different locations of these eigenvalues in Fig. 4(a), these two nodes are as similar as possible in terms of their state-space vector, as summarized in Table II. Both have $Q > 0$ and $R < 0$, with the latter meaning that normal strain production is negative and normal enstrophy production is positive (the nodes represent a developing flow structure with a closed streamline in the Lagrangian frame). There is only a single difference between these nodes, which is highlighted by the "(b)" superscript in the Table: One of these nodes has both the strain production, $-\det(\boldsymbol{S})$, and enstrophy production, $\mathrm{tr}(\boldsymbol{\Omega}^2\boldsymbol{S})$, negative (only the case for 3% of the flow where $Q > 0$ and $R < 0$ at this Reynolds number according to [42]), while the other has strain production negative and enstrophy production positive. That both of these nodes had strain production negative is noteworthy because, on average, this term must be positive to balance vortex stretching [43,44]. For both nodes, the signs of the production terms in row 4 are identical as are the relative magnitudes in row 5. Because $R < 0$ in row 1, the signs of $-\det(\boldsymbol{S}_B)$ and $\mathrm{tr}(\boldsymbol{\Omega}_B^2\boldsymbol{S}_B)$ must be negative and positive, respectively. Hence, with all terms in rows 4 and 5 the same for these two nodes, the change in sign for $\mathrm{tr}(\boldsymbol{\Omega}^2\boldsymbol{S})$ in row 3 must be small in magnitude and driven by $\mathrm{tr}(\boldsymbol{\Omega}_B^2\boldsymbol{S}_B)$ being relatively larger for the node associated with the square, but still retaining a ranking of second largest term in row 5. Thus, the physics captured by the nodes given by the diamond and the square is as similar as is possible while still leading to a distinct state for the state-space vector. These network nodes are also unusual, not only because of the negative strain production, but because the largest magnitude production term (row 5) is $|\det(\boldsymbol{S}_C)|$ (this is the third term listed in the first column of the table, therefore corresponding to the 1 in "[4,2,1,3]" in the second and third columns). This term is close to zero on average and typically the smallest magnitude term [39]. Hence, the complexity in the dynamics captured by the pseudospectral frontier reflects relatively unusual turbulent flow physics.

There are two distinct maxima for the EGC network, as shown by the black triangles in Fig. 4(e). These are closer in terms of their θ_0 values than for the DNS results, but the

eigenvalues that seem to be driving these responses, given by blue triangles in Fig. 4(c), are less similar to each other (in terms of the weighting of the original network nodes on their eigenvectors) than for the DNS results, as shown in the right-hand column of Fig. 5. While they were close neighbors in Fig. 4(c), all four are dominated by different network nodes, and these differ to those identified for the DNS. The nature of the state-space vector for each of these nodes is given in Table II and they represent very different physical states from the nodes highlighted for the DNS. The plus and cross nodes have $Q > 0$ again, but $R > 0$ (the vortex is waning because the diffence between strain production and enstrophy production is positive). The nodes highlighted by the star and asterisk have $Q < 0$, but $\Delta > 0$. That is, the flow structure has gained sufficient rotation to develop a closed streamline in the Lagrangian frame, but not yet enough for the enstrophy to exceed the total strain. Differences within these pairs of nodes are also clear. For example, the plus and cross differ on row 4: the former has both non-normal and interaction production positive, while both are negative for the latter. In contrast, the nodes given by the star and asterisk have the same signs on row 4, but differ on row 5 because the magnitudes of the terms from row 4 change in their ranking. This then affects the signs in row 3 as a consequence of the relation between these terms,

$$\begin{aligned} -\det(\boldsymbol{S}) &= -\det(\boldsymbol{S}_B) + \mathrm{tr}(\boldsymbol{\Omega}_C{}^2\boldsymbol{S}_B) - \det(\boldsymbol{S}_C), \\ \mathrm{tr}(\boldsymbol{\Omega}^2\boldsymbol{S}) &= \mathrm{tr}(\boldsymbol{\Omega}_B^2\boldsymbol{S}_B) + \mathrm{tr}(\boldsymbol{\Omega}_C{}^2\boldsymbol{S}_B) - \det(\boldsymbol{S}_C). \end{aligned} \tag{24}$$

In summary, network directedness expressed in terms of $d_\epsilon(\theta_0)$ leads to the identification of two nodes in the DNS network with very similar properties even though the associated eigenvalues sit in different parts of the complex plane. These nodes are unusual in having the turbulence production dominated by the purely non-normal term in row 5 of Table II and imply that the non-normal (shearing) processes play an important role in structuring the relative directedness for Lagrangian turbulence. The EGC model struggles to capture this subtle aspect of the dynamics. This result is interesting because a comparison between these networks using more conventional network metrics by [45] highlighted the significance of $\|\boldsymbol{\Omega}_C\|^2$ (the non-normal contribution to enstrophy and strain) rather than the production dynamics.

VI. CONCLUSION

The directed graph Laplacian (DGL) bounds all of the eigenvalues for a real-valued network to a half disc in the complex plane with unit radius. The pseudospectrum provides additional information on the structure of the network, but by virtue of being a continuous field, can be hard to interpret. In this study, we have proposed a way to threshold the pseudospectrum such that the eigenvalues are contained within the "containing frontier," denoted by $z_\tau(\boldsymbol{\mathcal{L}})$. This frontier is compared to that derived from the Laplacian for a variant of the original network with the non-normality removed, $\boldsymbol{\mathcal{L}}_n$. A visual representation of the difference between $z_\tau(\boldsymbol{\mathcal{L}})$ and $z_\tau(\boldsymbol{\mathcal{L}}_n)$ is shown for various networks in Figs. 1(b) and 1(e), Fig. 2 and Fig. 4. Because the underlying pseudospectral surface is highly nonlinear, it is best to quantify the separation between the two frontiers in terms of ϵ, which gives a relative measure of directedness, $d_\epsilon(\theta_0)$, as defined in (16).

Having shown our approach is consistent with the intuitive behavior of a network formed from a cyclic permutation adjacency matrix, we used a network of social interaction to vary the relative directedness of the network, as shown in Figs. 2 and 3. Because $d_\epsilon(\theta_0)$ encapsulates the whole frontier, it is not overly affected by changes to one of the frontiers in a specific region, as happens for the distance between pseudospectral ordinates, β_{ex}, in Fig. 3. Having verified our method, it subsequently underpinned a more extensive analysis for a network of the dynamics of homogeneous, isotropic turbulence [9,45] built from a direct numerical simulation (DNS) of the Navier-Stokes equation and a stochastic model for these dynamics [40]. We found two maxima for $d_\epsilon(\theta_0)$ at very different angles θ_0 from the displaced origin for the DNS case. For each maximum, there were two eigenvalues that appeared to dictate their behavior and these were not the eigenvalues with the largest imaginary part. Investigating how strongly the network nodes were weighted on the eigenvectors for these eigenvalues, we found the same two nodes dominated and these were as similar as possible in terms of the state-space vector used to define the vertices in the network, differing in only one attribute as shown on row 3 of Table II. In terms of the flow physics, these nodes represented developing flow structures with a closed streamline in the Lagrangian frame of reference, but were unusual because the largest magnitude production term was that purely based on the tensor non-normality, which is typically either the smallest or second smallest in magnitude [39]. Non-normal terms do not feature in the restricted Euler model for the dynamics of the velocity gradient tensor [46], meaning that more sophisticated closure models have been developed to capture these effects. Using one such model, the enhanced Gaussian closure [40], we found clear differences in the qualitative nature of the Laplacian pseudospectra (Fig. 4) as well as quantitative differences in τ_ϵ and $d_\epsilon(\theta_0)$, and the physics represented by the eigenvalues driving these behaviors (Table II).

Based on the results presented here, it is envisaged that these tools for measuring network absolute and relative directedness will be of use to engineers and scientists in a diverse range of fields who work with directed networks and require a means to determine the structure of the associated directed graph Laplacian or wish to use this to unveil aspects of the underpinning physics. Evaluating the set of values $d_\epsilon(\theta_0)$ is more time consuming than using simple scalar quantities, but its potential value has been shown for our turbulence example. To try to reduce the computations required and retain efficiency for larger networks, our definition of the containing pseudospectral frontier is based on values on the real line, rather than evaluating the pseudospectrum over the full complex plane.

ACKNOWLEDGMENTS

C.J.K. is grateful to the Leverhulme Trust International Fellowship 2023-014 that supported this research. He was kindly hosted by Prof. Michael Wilczek in the Department of Theoretical Physics at the University of Bayreuth and Prof. Blair Johnson and Prof. Paola Passalacqua at the Environmental and Water Resources Engineering Group, University

of Texas at Austin, where a significant part of this research was undertaken.

DATA AVAILABILITY

The data that support the findings of this article are openly available [12,36,47].

APPENDIX A: METRICS FOR CHARACTERIZING SPECTRA AND PSEUDOSPECTRA

The field of values or numerical range, $W(\boldsymbol{\mathcal{L}})$, is the set of all the Rayleigh coefficients,

$$w(\theta) = \frac{x(\theta)^* \boldsymbol{\mathcal{L}} x(\theta)}{x(\theta)^* x(\theta)}, \tag{A1}$$

with $\|x(\theta)\| = 1$ for angles $\theta \in \{0, 2\pi\}$. Rotating $\boldsymbol{\mathcal{L}}$ by θ gives

$$\boldsymbol{\mathcal{L}}_{(\theta)} = \boldsymbol{\mathcal{L}} e^{i\theta}, \tag{A2}$$

which may then be symmetrized according to $0.5(\boldsymbol{\mathcal{L}}_{(\theta)} + \boldsymbol{\mathcal{L}}^*_{(\theta)})$. The eigenvector corresponding to the eigenvalue with the smallest real part for this symmetrized Laplacian matrix is then used to define $x(\theta)$ [48]. From the field of values, one can define the numerical abscissa,

$$\alpha(\boldsymbol{\mathcal{L}}) = \sup_{z \in W(\boldsymbol{\mathcal{L}})} \mathrm{Re}(z), \tag{A3}$$

and the pseudospectral abscissa reexpresses (A3) in terms of the pseudospectrum rather than the field of values,

$$\alpha_\epsilon(\boldsymbol{\mathcal{L}}) = \sup_{z \in \Lambda_\epsilon(\boldsymbol{\mathcal{L}})} \mathrm{Re}(z). \tag{A4}$$

A pseudospectral radius may then be defined as the point within $\Lambda_\epsilon(\boldsymbol{\mathcal{L}})$ that lies furthest from the origin,

$$\rho_\epsilon(\boldsymbol{\mathcal{L}}) = \sup_{z \in \Lambda_\epsilon(\boldsymbol{\mathcal{L}})} |z|. \tag{A5}$$

While, in principle, ρ_ϵ appears as if it will help characterize directedness of the DGL, the difficulty concerns the nature of the eigenvalues for these Laplacians. The DGL has eigenvalues that are bounded on the real line between 0 and 2 and the cyclic permutation matrix considered in the main body of this paper highlights the issue. The DGL for this matrix has all the eigenvalues on the edge of a unit circle with a center at $1 + 0i$ [Fig. 1(e)]. Hence, the greatest distance from the origin to the bounds on the eigenvalues will be along the real line, meaning that for many networks, to high probability, $\rho_\epsilon(\boldsymbol{\mathcal{L}}) = \alpha_\epsilon(\boldsymbol{\mathcal{L}})$. A more appropriate alternative is the pseudospectral ordinate [24],

$$\beta_\epsilon(\boldsymbol{\mathcal{L}}) = \sup_{z \in \Lambda_\epsilon(\boldsymbol{\mathcal{L}})} \mathrm{Im}(z), \tag{A6}$$

which is used in this paper as a metric for directedness.

APPENDIX B: NUMERICAL PROCEDURE TO OBTAIN z_τ

The approach we follow to derive z_τ largely follows Refs. [33,34]. For each angle $\theta_j \in \{0, \pi\}$, the Hamiltonian matrix $\boldsymbol{H}$ and an orientation matrix $\boldsymbol{K}_j$ are defined as

$$\begin{aligned} \boldsymbol{H} &= \begin{bmatrix} -\epsilon_\tau \boldsymbol{I} & \boldsymbol{\mathcal{L}} \\ \boldsymbol{\mathcal{L}}^* & -\epsilon_\tau \boldsymbol{I} \end{bmatrix}, \\ \boldsymbol{K}_j &= \begin{bmatrix} \boldsymbol{O} & [\cos(\theta_j) + i \sin(\theta_j)]\boldsymbol{I} \\ [\cos(\theta_j) - i \sin(\theta_j)]\boldsymbol{I} & \boldsymbol{O} \end{bmatrix}. \end{aligned} \tag{B1}$$

One then seeks the generalized eigenvalues that are a solution to $\boldsymbol{H} - \lambda_{H,K}\boldsymbol{K}_j$ and are real valued, to within some small tolerance on the imaginary part. If such eigenvalues exist, then ϵ_τ is a singular value of $\boldsymbol{\mathcal{L}} - e^{-i\theta}\boldsymbol{I}$. With the set of eigenvalues that fulfill this criterion as $\Lambda_{H,K}(\theta)$, one has that

$$z_\tau(\theta) = \sup\ \mathrm{Re}[\boldsymbol{\Lambda}_{H,K}(\theta)]. \tag{B2}$$

As noted in the main text, there are practical difficulties working with θ, leading to our use of a displaced origin θ_0. Our sampling for θ_0 in the numerical method is adaptive. We initially choose θ_0 as distributed regularly on the interval from 0 to π and then refine this, where the change in z_τ for consecutive choices of θ_0 is large. Our refinement threshold is based on concepts in Ref. [49]: We consider the change of z_τ from the ith to the $(i+1)$th value of θ_0 and then estimate the threshold θ_T using the median absolute deviation (MAD),

$$\begin{aligned} \theta_T &= \frac{\sqrt{2\log N}}{0.6745}\mathrm{MAD}(\hat{z}_\tau(\theta_0)) \\ \mathrm{MAD}(\hat{z}_\tau(\theta_0)) &= \langle |\hat{z}_\tau(\theta_0)| \rangle_{50} \\ \hat{z}_\tau(\theta_0) &= |z_\tau(\theta_0[i+1]) - z_\tau(\theta_0[i])|. \end{aligned} \tag{B3}$$

We terminate refinement of the angles when all $\hat{z}_\tau(\theta_0) < \theta_T$.

[1] A. Bombelli, B. F. Santos, and L. Tavasszy, Analysis of the air cargo transport network using a complex network theory perspective, Trans. Res. E: Logist. Trans. Rev. **138**, 101959 (2020).

[2] M. Zhang, T. Huang, Z. Guo, and Z. He, Complex-network-based traffic network analysis and dynamics: A comprehensive review, Physica A **607**, 128063 (2022).

[3] R. Su, B. Chen, S. Wang, and C. Duan, Energy technical resilience assessment based on complex network analysis - A case study of China, Appl. Energy **364**, 123231 (2024).

[4] R. L. Shreve, Infinite topologically random channel networks, J. Geol. **75**, 178 (1967).

[5] E. D. Mainas, The analysis of criminal and terrorist organisations as social network structures: A quasi-experimental study, Intl. J. Police Sci. Manag. **14**, 264 (2012).

[6] J. Senk, B. Kriener, M. Djurfeldt, N. Voges, H.-J. Jiang, L. Schüttler, G. Gramelsberger, M. Diesmann, H. E. Plesser, and S. J. van Albada, Connectivity concepts in neuronal network modeling, PLOS Comput. Biol. **18**, e1010086 (2022).

[7] M. K. P. So, A. M. Y. Chu, A. Tiwari, and J. N. L. Chan, On topological properties of COVID-19: Predicting and assessing pandemic risk with network statistics, Sci. Rep. **11**, 5112 (2021).

[8] Y. Zou, R. V. Donner, N. Marwan, J. F. Donges, and J. Kurths, Complex network approaches to nonlinear time series analysis, Phys. Rep. **787**, 1 (2019).

[9] C. J. Keylock and M. Carbone, Complex network approach to turbulent velocity gradient dynamics: High- and low-probability Lagrangian paths, Phys. Rev. Fluids **10**, 054606 (2025).

[10] F. Chung, *Spectral Graph Theory* (American Mathematical Society, Providence, RI, 1997).
[11] F. R. K. Chung, Laplacians and the Cheeger inequality for directed graphs, Ann. Comb. **9**, 1 (2005).
[12] Y. Li and Z.-L. Zhang, Digraph Laplacian and the degree of asymmetry, Internet Math. **8**, 381 (2012).
[13] M. Asllani, R. Lambiotte, and T. Carletti, Structure and dynamical behavior of non-normal networks, Sci. Adv. **4**, eaau9403 (2018).
[14] L. N. Trefethen and M. Embree, *Spectra and Pseudospectra: The Behavior of Non-normal Matrices and Operators* (Princeton University Press, Princeton, NJ, 2005).
[15] F. Göbel and A. Jagers, Random walks on graphs, Stochast. Proc. Appl. **2**, 311 (1974).
[16] M. Fiedler, A property of eigenvectors of nonnegative symmetric matrices and its applications to graph theory, Czech. Math. J. **25**, 619 (1975).
[17] F. Chung and S.-T. Yau, Discrete Green's functions, J. Comb. Theory Ser. A **91**, 191 (2000).
[18] A. Barabási and R. Albert, Emergence of scaling in random networks, Science **286**, 509 (1999).
[19] P. Erdös and A. Rényi, On the evolution of random graphs, Mat. Kutató Int. Közl. **5**, 17 (1960).
[20] D. J. Watts and S. H. Strogatz, Collective dynamics of "small-world" networks, Nature (London) **393**, 440 (1998).
[21] A. Vázquez, R. Pastor-Satorras, and A. Vespignani, Large-scale topological and dynamical properties of the internet, Phys. Rev. E **65**, 066130 (2002).
[22] V. M. Eguìluz, D. R. Chialvo, G. A. Cecchi, M. Baliki, and A. V. Apkarian, Scale-free brain functional networks, Phys. Rev. Lett. **94**, 018102 (2005).
[23] P. Henrici, Bounds for iterates, inverses, spectral variation and fields of values of non-normal matrices, Numer. Math. **4**, 24 (1962).
[24] S. C. Reddy, P. J. Schmid, and D. S. Henningson, Pseudospectra of the Orr-Sommerfeld operator, SIAM J. Appl. Math. **53**, 15 (1993).
[25] L. N. Trefethen, A. E. Trefethen, S. C. Reddy, and T. A. Driscoll, Hydrodynamic stability without eigenvalues, Science **261**, 578 (1993).
[26] S. A. Orszag, Accurate solution of the Orr-Sommerfeld equation, J. Fluid Mech. **50**, 689 (1971).
[27] L. N. Trefethen, Computation of pseudospectra, Acta Numer. **8**, 247 (1999).
[28] T. G. Wright and L. N. Trefethen, Pseudospectra of rectangular matrices, IMA J. Numer. Anal. **22**, 501 (2002).
[29] N. J. Higham, Matrix nearness problems and applications, in *Applications of Matrix Theory*, edited by M. J. C. Gover and S. Barnett (Oxford University Press, Oxford, 1989), pp. 1–27.
[30] R. W. Daniel and B. Kouvaritakis, The choice and use of normal matrix approximations to transfer-function matrices of multivariable control systems, Intl. J. Control **37**, 1121 (1983).
[31] C.-Y. Kao, U. Jönsson, and H. Fujioka, Characterization of robust stability of a class of interconnected systems, Automatica **45**, 217 (2009).
[32] I. Schur, On the characteristic roots of a linear substitution with an application to the theory of integral equations, Math. Ann. **66**, 488 (1909).
[33] R. Byers, A bisection method for measuring the distance of a stable matrix to the unstable matrices, SIAM J. Sci. Stat. Comput. **9**, 875 (1988).
[34] E. Mengi and M. L. Overton, Algorithms for the computation of the pseudospectral radius and the numerical radius of a matrix, IMA J. Numer. Analys. **25**, 648 (2005).
[35] R. Rossi and N. Ahmed, The network data repository with interactive graph analytics and visualization, in *Proceedings of the AAAI Conference on Artificial Intelligence* (Association for the Advancement of Artificial Intelligence, Washington, DC, 2015), Vol. 29, pp. 4292–4293.
[36] Network data repository, https://networkrepository.com/bn-cat-mixed-species-brain-1.php.
[37] S. Jiang, J. A. Lu, J. Zhou, and Q. Dai, Fiedler value: The cumulated dynamical contribution value of all edges in a complex network, Phys. Rev. E **109**, 054301 (2024).
[38] D. Knoke and J. H. Kuklinski, *Network Analysis* (Sage, London, 1982).
[39] C. J. Keylock, The Schur decomposition of the velocity gradient tensor for turbulent flows, J. Fluid Mech. **848**, 876 (2018).
[40] M. Wilczek and C. Meneveau, Pressure Hessian and viscous contributions to velocity gradient statistics based on Gaussian random fields, J. Fluid Mech. **756**, 191 (2014).
[41] L. Chevillard, C. Meneveau, L. Biferale, and F. Toschi, Modeling the pressure Hessian and viscous Laplacian in turbulence: Comparisons with direct numerical simulation and implications on velocity gradient dynamics, Phys. Fluids **20**, 101504 (2008).
[42] C. J. Keylock, Turbulence at the Lee bound: Maximally non-normal vortex filaments and the decay of a local dissipation rate, J. Fluid Mech. **881**, 283 (2019).
[43] R. Betchov, An inequality concerning the production of vorticity in isotropic turbulence, J. Fluid Mech. **1**, 497 (1956).
[44] M. Carbone and M. Wilczek, Only two Betchov homogeneity constraints exist for isotropic turbulence, J. Fluid Mech. **948**, R2 (2022).
[45] C. J. Keylock and M. Carbone, Communities for the Lagrangian dynamics of the turbulent velocity gradient tensor: A network participation approach, Physica D **481**, 134826 (2025).
[46] B. J. Cantwell, Exact solution of a restricted Euler equation for the velocity gradient tensor, Phys. Fluids A **4**, 782 (1992).
[47] Johns Hopkins turbulence database, https://turbulence.idies.jhu.edu/home; H. Yu, K. Kanov, E. Perlman, J. Graham, E. Frederix, R. Burns, A. Szalay, G. Eyink, and C. Meneveau, Studying Lagrangian dynamics of turbulence using on-demand fluid particle tracking in a public turbulence database, J. Turbul. **13**, 1 (2012); Y. Li, E. Perlman, M. Wan, Y. Yang, C. Meneveau, R. Burns, S. Chen, A. Szalay, and G.Eyink, A public turbulence database cluster and applications to study Lagrangian evolution of velocity increments in turbulence, *ibid.* **9**, 31 (2008).
[48] C. R. Johnson, Numerical determination of the field of values of a general complex matrix, SIAM J. Numer. Anal. **15**, 595 (1978).
[49] D. L. Donoho and I. M. Johnstone, Adapting to unknown smoothness via wavelet shrinkage, J. Am. Stat. Assoc. **90**, 1200 (1995).